Mantle cloaking using thin patterned metasurfaces

Pai-Yen Chen and Andrea Alù*

The University of Texas at Austin, Department of Electrical and Computer Engineering, Austin, Texas, 78712, USA

(Received 25 May 2011; revised manuscript received 7 September 2011; published 10 November 2011)

We explore in detail the concept of mantle cloaking, showing that a single, ultrathin, conformal metasurface may drastically suppress the scattering from planar [one-dimensional (1D)], cylindrical [two-dimensional (2D)], and/or spherical [three-dimensional (3D)] objects. We propose realistic designs that may realize this concept at radio (RF) or far-infrared (FIR) frequencies. In addition we discuss properties and physical insights of this cloaking functionality compared to other available techniques involving bulk metamaterials, showing exciting potentials in terms of ultralow-profile, light-weight, and bandwidth of operation. These results may be of great interest for low-observability, camouflaging, noninvasive probing, and low-noise communication applications.

DOI: 10.1103/PhysRevB.84.205110 PACS number(s): 42.70.−a, 33.20.Fb, 42.50.Gy, 42.79.−e

I. INTRODUCTION

In recent years considerable attention has been focused on the concept and realization of electromagnetic invisibility cloaks as one of the most exciting applications of metamaterials.[1–14] It has been theoretically shown and experimentally verified in several scenarios that the anomalous wave interaction of artificial materials and metamaterials may be tailored to largely reduce the overall visibility of a given object in different frequency regions, spanning radio-frequencies (RF),[3,11] infrared, and visible light.[15–20] Thanks to recent advances in micro/nanofabrication, passive[1–24] and active[25,26] approaches to metamaterial cloaking have been successfully developed,[1–30] envisioning a variety of fascinating applications that include not only camouflaging and low-observability,[1–6] but also noninvasive sensing[9,22] and low-noise communications.[27,28]

Transformation-based cloaking techniques[2–4] are arguably the most popular at the moment, and their experimental realization has been pursued with some success in RF,[3] near-infrared, and visible frequencies.[15–20] This cloaking technique relies on specific anisotropy and inhomogenity profiles of bulk metamaterials that can bend the electromagnetic wave around a given region, making it effectively invisible. An ideal transformation-based cloak can completely isolate the cloaked object, as if the cloak and the internal region do not exist from the electromagnetic standpoint. Plasmonic cloaking,[1,7–11,29,30] in contrast, is based on the scattering cancelation properties of low- or negative-index metamaterials that may produce an "anti-phase" scattered wave, canceling most of the scattered fields and thus effectively cloaking a given object. Alternative techniques based on other exotic properties of bulk metamaterials have also been successfully proposed and investigated in the context of cloaking and invisibility.

Even if the theoretical foundations of all these cloaking techniques involving metamaterials are well understood, the practical realization of these devices, based on currently available metamaterial technology, is far from ideal, and the experiments reported at present have ensured only limited scattering reduction, far from the theoretical predictions. This is mainly due to the inherent difficulty in realizing bulk metamaterials as collections of small inclusions with required exotic bulk properties that may be treated as a continuum.[31,32] These limitations are particularly evident for transformation-based cloaks, since they require complex and precise inhomogeneity profiles that may be hard to realize using arrays with finite granularity. In addition several of these cloaking techniques require an overall thickness that is comparable with the size of the region to be cloaked, which may cause bandwidth limitations and increased sensitivity to realistic material loss.[33,34]

In an attempt to relieve the limitations of cloaks based on bulk metamaterials, we have recently proposed the concept of mantle cloaking, showing that an ultrathin patterned conducting surface may successfully reduce the overall scattering from a given object[23,24] without relying on exotic bulk material properties. This may be realized within established technology at RF or far-infrared (FIR) frequencies using metasurfaces or frequency-selective surfaces (FSS),[35–37] which are currently used for a wide range of different applications, ensuring a promising venue to practical realization and robust performance. Our preliminary theoretical investigations of this cloaking technique[23,24] were limited to the ideal assumption of uniform and dispersionless surface impedance, which is approximately valid over a moderately broad range of frequencies for FSS. Here, we extensively discuss physical insights, robustness, and practical designs of mantle cloaks in several one- (1D), two- (2D), and three-dimensional (3D) geometries (see Fig. 1), considering their realistic frequency dispersion and presence of losses. In addition we propose practical metasurface designs based on established FSS technology. We mainly focus on canonical objects, i.e., planar slabs, cylinders, and spheres, but this concept may be straightforwardly extended to arbitrary shapes [Fig. 1(d)]. Even if our designs are here focused on RF, extensions to the THz and infrared regions are feasible using similar concepts, a frequency region for which metamaterial cloaking is currently unexplored.

II. 1D GEOMETRY: PLANAR MANTLE CLOAKS

A thin conducting surface periodically patterned over a scale much smaller than the wavelength of operation may be effectively described by its averaged surface impedance, $Z_s = R_s - iX_s$,[35] which relates the averaged tangential electric field at the surface to the averaged surface current density as $\mathbf{E}_{\tan} = Z_s\mathbf{J}$. Here, and in the following, an $e^{-i\omega t}$ time

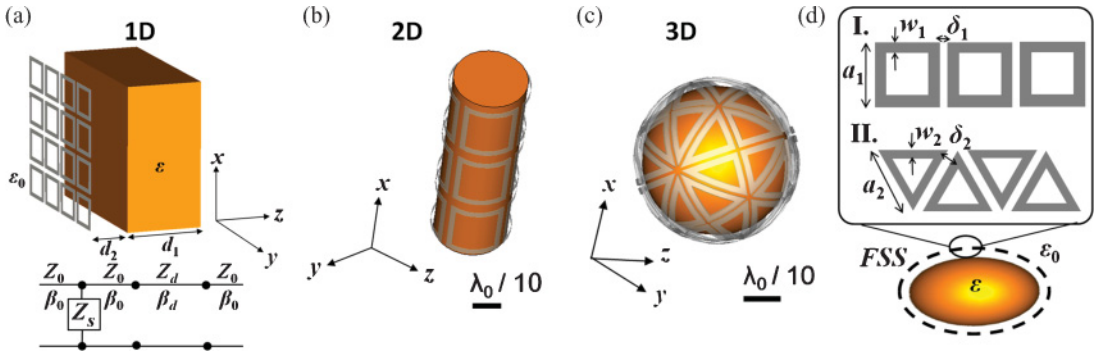

FIG. 1. (Color online) Mantle cloaks for (a) a planar dielectric slab (1D); (b) a dielectric infinite cylinder (2D); and (c) a dielectric sphere (3D). (d) Metasurface designs analyzed in this study.

dependence is assumed. The surface resistance $R_s \geqslant 0$ is associated to absorption, and therefore a lossless metasurface has a purely imaginary impedance. The surface reactance X_s may assume a wide range of values as a function of the metasurface geometry and the frequency of operation. As discussed in Ref. 23, ultrathin mantle cloaks may be realized by properly selecting the value of X_s.

In this section in order to provide physical insights into the functionality of mantle cloaking, we start by considering the simplest mantle cloak geometry, limited to a 1D problem [Fig. 1(a)]: a dielectric planar slab with finite thickness d_1, cloaked by a metasurface screen placed at distance d_2. The scattering properties of this geometry may be analyzed using a transmission-line (TL) model, as in the inset of Fig. 1(a), where β_i, η_i represent the wave number and characteristic impedance of the ith-TL segment, respectively. Provided that the real part of the input admittance at a given distance d_2 from the slab is equal to the background line admittance $\eta_0^{-1} = (377\Omega)^{-1}$, it is possible to match the line and completely cancel the reflected wave by suppressing the input susceptance with a suitably chosen value of X_s. A properly designed planar metasurface, consisting of subwavelength patterns on a conducting screen, may provide the required surface impedance at the frequency of interest.[35] For thin slabs, for which $\beta_d d_1, \beta_0 d_2 \ll \lambda_0$, the required surface reactance X_s and separation distance d_2 may be obtained in closed forms as

$$X_s = \frac{\eta_0^2 \eta_d}{\beta_1 d_1 \left(\eta_0^2 - \eta_d^2\right)}, \qquad d_2 = \frac{\eta_d \left(1 + \sqrt{1 + \beta_d^2 d_1^2}\right)}{\eta_0 \beta_0 \beta_d d_1}. \tag{1}$$

In Fig. 2 we compare analytical results (solid line) with full-wave simulations[38] (dashed line) of a properly designed planar FSS that may realize the required X_s at the frequency of interest. In this example the cloaked object is a dielectric slab with thickness $d_1 = \lambda_0/10$ and relative permittivity $\varepsilon = 10$, where λ_0 is the free-space wavelength at the design frequency. For our analytical calculations we have assumed a dispersionless ideal reactive surface with optimal design parameters obtained from the TL model: $d_2 = \lambda_0/31$ and $X_s = 144.8\Omega$. The full-wave simulations consider a realistic mantle cloak placed at the same distance d_2, formed by a metasurface geometry with unit cell depicted in Fig. 1(d): a type-I FSS with design parameters $a_1 = \lambda_0/10$, $w_1 = \lambda_0/100$. The FSS thickness is $t = \lambda_0/400$, much thinner than any conceivable metamaterial cloak.

Excellent agreement is observed in Fig. 2 between analytical results and full-wave simulations around the design frequency f_0, with a small discrepancy due to the natural dispersion of the realistic metasurface. In the uncloaked scenario the reflection dip at higher frequency is associated with a classic Fabry-Perot resonance,[24] which is based on a different tunneling mechanism compared to the transparency at lower frequency: a Fabry-Perot etalon is characterized by tunneling with large field amplification inside the slab and associated flip in the phase distribution, whereas the 1D cloaking presented here is obtained via destructive interference of the reflected fields from the slab and the FSS, which may arise also in a quasistatic scenario and does not imply field amplification or sharp variations of the transmitted phase.

It should be noticed that other recently proposed 1D cloaks, such as planar carpet cloaks,[16–20] can only suppress the scattering from a bump on a planar reflector, rather than making the whole reflector transparent. In the present scenario the total absence of reflection is based on the cancelation of scattering due to destructive interference between the FSS and the planar slab, and it is effective as long as the object to be cloaked is penetrable and low-loss.

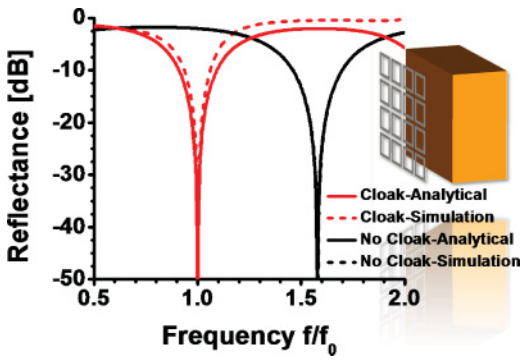

FIG. 2. (Color online) Frequency variation of the reflectance for a dielectric slab with thickness $d_1 = \lambda_0/10$ and relative permittivity $\varepsilon = 10$, covered by a planar metasurface with suitable separation d_2 and reactance X_s. We compare analytical results for an ideal value of surface impedance with full-wave simulations of a suitably designed FSS, as shown in the inset.

Most metamaterial cloaks at present operate near the inclusion resonances to realize extreme metamaterial permittivity and/or permeability, consistent with the requirements of transformation-based cloaks.[2–4] These resonances usually result in strong frequency dispersion and sensitivity to losses. However, the scattering cancelation mechanism applied here is inherently nonresonant, and it is applicable to planar slabs of any thickness. Compared to conventional antireflection coatings, the metasurface here may have a much lower profile, possibly conformal to the object or a small fraction of the wavelength thick. In the quasistatic limit, the closed-form design expressions [Eq. (1)] well approximate the optimal design formulas. Finally, it should be mentioned that as long as the patterns in the FSS screen are subwavelength and the slab is not too thick, as in the example of Fig. 2, the metasurface response is inherently robust to variations in the incidence angle.[39,40] Figure 3 shows (a) analytical results and (b) full-wave simulations for the cloaked dielectric slab in Fig. 2 under TM illumination for various incidence angles θ_i. It is evident from these examples how an ultrathin metasurface may drastically suppress the reflection from a dielectric slab at the desired frequency by the means of destructive interference. A small difference between the analytical results and simulations is due to the FSS frequency dispersion. The dependence of the reflection dip on the incidence angle is mainly associated with the distance between slab and FSS and may be reduced by filling the gap with a high dielectric constant material (not shown here). This makes the phase variation along the propagation direction and the optimal condition for d_2 less sensitive to the incidence angle. Similar concepts may be used for 2D and 3D objects, as we discuss in the next sections.

III. 2D GEOMETRY: CYLINDRICAL MANTLE CLOAKS

In analogy with the previous example, the concept of metasurface cloaking may be extended to 2D elongated objects [Fig. 1(b)]. As a first example, we consider the 2D version of the previous example: a dielectric infinite cylinder with relative permittivity $\varepsilon = 10$ and diameter $2a = \lambda_0/5$, covered by an ultrathin concentric mantle cloak with radius a_c. For any arbitrary incidence angle, the plane wave scattering may be analytically calculated by forcing a discontinuity on the tangential magnetic field at the surface of the mantle cloak, which is proportional to the averaged current induced on the surface, resulting in the boundary condition at $r = a_c$:

$$\mathbf{E}_{\tan}|_{r=a} - Z_s \times \hat{\mathbf{r}} \times (\mathbf{H}_{\tan}|_{r=a^+} - \mathbf{H}_{\tan}|_{r=a^-}) = 0. \quad (2)$$

The impinging electric and magnetic fields may be expanded in terms of the superposition of cylindrical harmonics centered along the object axis ($z-$axis in the associated cylindrical reference system). Consider a normally incident transverse-magnetic (TM) plane wave impinging with magnetic field polarized orthogonal to the cylinder axis. The scattered fields may be expanded in terms of cylindrical harmonics with complex scattering coefficients c_l^{TM} and c_l^{TE}, which may be written in the notation of Ref. 41 as

$$c_l^{\mathrm{TE}} = -\frac{P_l^{\mathrm{TE}}}{P_l^{\mathrm{TE}} + i\,Q_l^{\mathrm{TE}}}, \quad c_l^{\mathrm{TM}} = -\frac{P_l^{\mathrm{TM}}}{P_l^{\mathrm{TM}} + i\,Q_l^{\mathrm{TM}}}, \quad (3)$$

where here, using Eq. (2),

$$P_l^{\mathrm{TM}} = \begin{bmatrix} J_l(ka) & J_l(k_0a) & Y_l(k_0a) & 0 \\ k\,J_l'(ka)/\mu & k_0 J_l'(k_0a) & k_0 Y_l'(k_0a) & 0 \\ 0 & J_l(k_0a_c) & Y_l(k_0a_c) & J_l(k_0a_c) \\ 0 & \begin{matrix} J_l'(k_0a_c) - \\ -i\omega\mu_0 J_l(k_0a_c)/(k_0Z_s) \end{matrix} & \begin{matrix} Y_l'(k_0a_c) - \\ -i\omega\mu_0 Y_l(k_0a_c)/(k_0Z_s) \end{matrix} & J_l'(k_0a_c) \end{bmatrix},$$

$$Q_l^{\mathrm{TM}} = \begin{bmatrix} J_l(ka) & J_l(k_0a) & Y_l(k_0a) & 0 \\ k\,J_l'(ka)/\mu & k_0 J_l'(k_0a) & k_0 Y_l'(k_0a) & 0 \\ 0 & J_l(k_0a_c) & Y_l(k_0a_c) & Y_l(k_0a_c) \\ 0 & \begin{matrix} J_l'(k_0a_c) - \\ -i\omega\mu_0 J_l(k_0a_c)/(k_0Z_s) \end{matrix} & \begin{matrix} Y_l'(k_0a_c) - \\ -i\omega\mu_0 Y_l(k_0a_c)/(k_0Z_s) \end{matrix} & Y_l'(k_0a_c) \end{bmatrix}. \quad (4)$$

where $J(\cdot)$ and $Y(\cdot)$ are cylindrical Bessel functions,[42] k_0 and $k = k_0\sqrt{\varepsilon}$ are respectively the wave numbers in free space and in the object, and ε_0, μ_0 are the free-space permittivity and permeability. For transverse electric (TE) coefficients the dual of Eq. (4) may be easily derived. The total scattering width (SW) of the cylinder, as a general quantitative measure of its overall visibility at the frequency of interest, is given by the formula[43]

$$\sigma_{2\mathrm{D}} = \frac{4}{k_0} \sum_{l=-\infty}^{l=\infty} |c_l^{\mathrm{TM(TE)}}|^2. \quad (5)$$

If the l^{th} TM cylindrical scattering harmonic dominates the scattering of a given object, then its suppression is obtained by canceling the determinant P_l^{TM} with proper choice of a_c and X_s. This would lead to a large reduction of the overall scattering from the object, consistent with the results of the previous section in the planar scenario.[44] This scattering cancelation effect is consistent with the approach used in plasmonic cloaking,[1] even if here it is obtained with a single ultrathin surface rather than a bulk plasmonic metamaterial. In this 2D geometry the situation is complicated by the fact that several

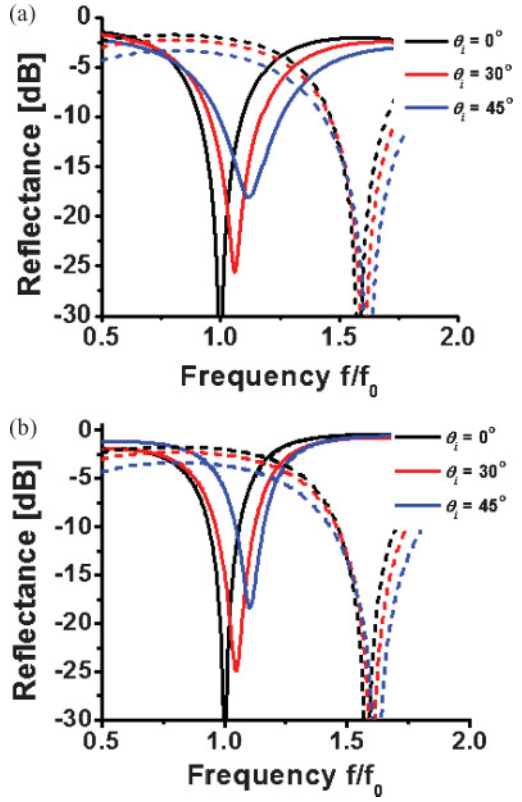

FIG. 3. (Color online) (a) Analytical results and (b) full-wave simulations for the frequency variation of the reflectance for the FSS setup of Fig. 2, varying the incidence angle θ_i.

scattering orders may dominate the scattering, especially for cylinders with larger cross-section. Due to the limited number of degrees of freedom, a single metasurface is effective in suppressing the scattering from a few scattering harmonics, implying that in this scheme only cylinders with geometrical cross-section comparable to the wavelength of excitation may be effectively cloaked. Extensions to multilayered mantle cloaks may be required for cloaking larger objects or realizing multifrequency cloaking, analogous to the plasmonic cloaking technique.[8]

Similar to the planar case, it is instructive to analyze how the cloaking conditions are simplified in the quasistatic limit, for which ka, $k_0 a_c \ll 1$ in Eq. (4). In this case the $l = 0$ harmonic dominates the overall scattering and closed-form cloaking conditions ($P_0 = 0$), for the TM and TE scattering coefficient are obtained as

$$\begin{aligned} \text{TM}: \quad X_s &= \frac{2}{\omega a \gamma \varepsilon_0 (\varepsilon - 1)}, \\ \text{TE}: \quad X_s &= \frac{\omega a \mu_0 (\gamma^2 (\mu - 1) + 1)}{4\gamma^3 (\mu - 1)}, \end{aligned} \tag{6}$$

where μ is the relative permeability of the cylinder to be cloaked and $\gamma = a/a_c$. As expected,[45] these quasistatic conditions do not depend on the total size of the object to be cloaked but rather on the ratio of radii γ, and the two polarizations are respectively associated to electric and magnetic effects.

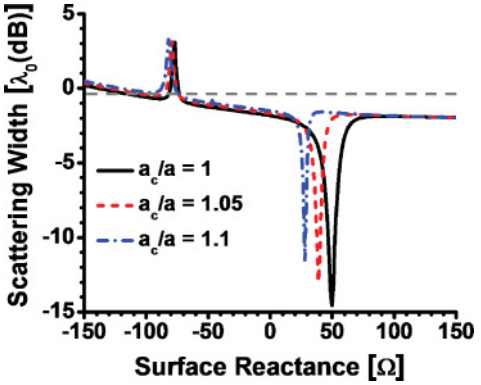

FIG. 4. (Color online) Variation of the total SW with the surface reactance of a mantle cloak for a dielectric infinite cylinder with diameter $2a = \lambda_0/5$ and relative permittivity $\varepsilon = 10$; different ratios a/a_c are presented.

Equation (6) shows that in the quasistatic limit TE and TM scattering from a 2D cylinder may be efficiently suppressed by properly tailoring the surface reactance of a concentric ultrathin mantle cloak. When the object size increases, dynamic formulas [Eq. (4)] may be used to precisely synthesize the mantle cloak. Figure 4 shows the variation of the total SW of a dielectric cylinder with $\varepsilon = 10$ and diameter $2a = \lambda_0/5$ versus the surface reactance of a mantle cloak for different ratios of radii a_c/a. The gray-dashed line in the figure indicates the scattering of the bare cylinder. It is observed that, for sufficiently large surface reactance values, the patterned surface has no influence on the SW, since the limit of no surface is given by $X_s \to \pm\infty$. However, with proper surface reactance values qualitatively consistent with Eq. (6) (although with some deviations due to the relatively large electrical size of the cylinder cross section), significant scattering reduction may be obtained with different cloak sizes, even in the limit of a conformal mantle cloak with $a_c = a$. It is found that over 96% and 91.5% reduction in total SW are respectively obtained by a conformal cloak and a cloak with radius $a_c = 1.1a$, with proper surface-reactance values ($X_s = 49.8\ \Omega$ for the conformal cloak and $X_s = 28\ \Omega$ for the one with $a_c = 1.1a$), despite the ultimately low profile of this surface impedance. Cloaking effects comparable to those achievable with metamaterials are obtained here without the need of bulk material properties but simply using an ultrathin metasurface. The physical mechanism that drives this cloaking phenomenon is in some sense consistent with the plasmonic cloaking technique;[1] both are based on the scattering cancelation principle. However, different from plasmonic cloaks, we do not require here a bulk negative polarization in the cloak. Instead, the mantle cloak tailors the induced current on its patterned surface to produce antiphase scattered fields.

Figure 5 shows the variation of total SW versus frequency for the cloaked cylinders presented in Fig. 3, choosing an ideal surface reactance that is constant with frequency and optimized to suppress the scattering at frequency of interest f_0. Due to the generality of Foster's reactance theorem, this assumption may not be considered valid over a wide frequency range for passive surfaces, but it may be a good approximation

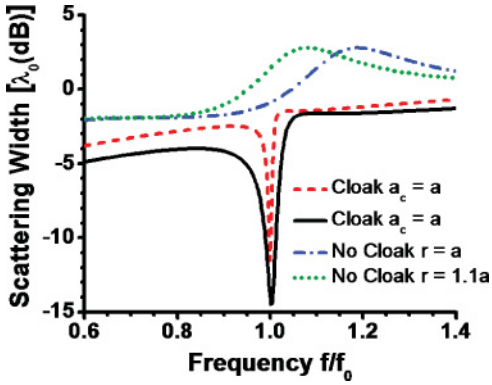

FIG. 5. (Color online) Total SW versus frequency for a dielectric cylinder with diameter $2a = \lambda_0/5$ and relative permittivity $\varepsilon = 10$ comparing cloaked and uncloaked scenarios. Different ratios a/a_c are presented, and in each case we use the optimal surface impedance cloak, as from Fig. 4, without considering frequency dispersion.

around the design frequency f_0, consistent with the previous 1D example in Fig. 2. The scattering is compared to uncloaked dielectric cylinders with radius a and a_c. Figure 5 confirms that a large scattering reduction may be obtained around the design frequency and over a moderately broad bandwidth when compared with uncloaked cylinders of comparable cross section.

Figure 6 shows the amplitude of electric field on the H plane for a dielectric infinite cylinder (a) with and (b) without a conformal ($a_c = a$) mantle cloak at the design frequency f_0. A plane wave excitation impinges from the left, and different panels in Fig. 6 are plotted in the same color scale for fair comparison. It is seen that the scattering may be significantly suppressed by the optimized mantle cloak, and a uniform field distribution is obtained even in the very near-field around the cylinder, despite its ultralow profile. Unlike ideal transformation-based cloaks that completely isolate their interior, the electromagnetic wave can penetrate the mantle cloak and the dielectric cylinder; therefore, the impinging signal may be detected by an observer or a sensor placed inside the mantle cloak.[9] This is particularly interesting for emerging applications in cloaked sensing, noninvasive probing, and low-interference communication.[9,22] Figure 6(e) shows the far-field radiation patterns for the cloaked and uncloaked dielectric cylinders, confirming that the cloak is effective in the far-field and for all observation angles.

In the previous examples we have focused on dielectric objects, but of equal importance for certain applications is the cloaking of impenetrable conducting materials.[29] In this scenario the wave cannot penetrate the object, and the causality requirements on passive devices make the cloaking more difficult to realize[33] and obviously impossible in the planar-1D geometry. In addition, due to the zero impedance of the cylinder surface, a gap between the shunt impedance of the mantle cloak and the conductor is necessary to avoid an electric short.

Figure 7 shows results analogous to Fig. 5 for a conducting cylinder of identical size, showing that significant scattering reduction may be obtained even for a metasurface very

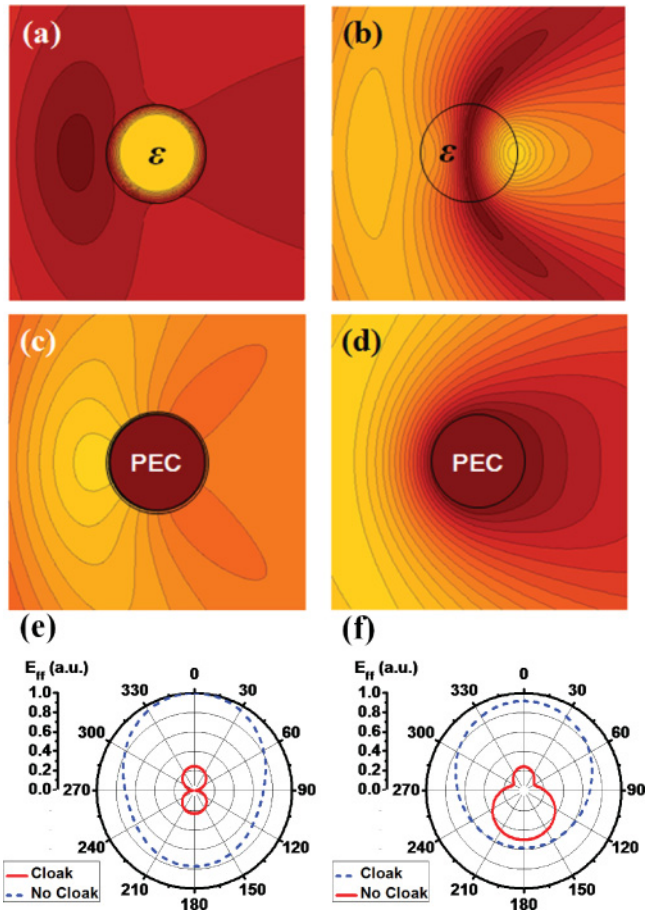

FIG. 6. (Color online) Near-field distributions of the amplitude of electric field on the H plane for a dielectric infinite cylinder (a) with and (b) without a conformal mantle cloak ($a_c = a$); a conducting infinite cylinder (c) with and (d) without a mantle cloak with radius $a_c = 1.05a$. Far-field radiation patterns for (e) a dielectric infinite cylinder with and without the conformal mantle cloak, as in (a); (f) a conducting infinite cylinder with and without the mantle cloak in (c).

close to the cylinder surface. For the case $a_c = 1.05a$, the optimal impedance is $X_s = -12\,\Omega$ and the calculated overall scattering reduction is about 86%, which is less than in the dielectric case, mainly due to contributions from high-order scattering orders.[41] Despite the object being impenetrable, an ultrathin mantle cloak holds the promise to significantly suppress the overall scattering in all directions, as can be seen comparing the far-field patterns for the cloaked and uncloaked conducting cylinders in Fig. 6(f). Such results represent an improvement over the use of plasmonic cloaks in suppressing the scattering from conducting cylinders,[41] possibly due to the low profile of this cloaking configuration. Figures 6(c) and 6(d) show similar field plots as in Figs. 6(a) and 6(b) but for this conducting scenario. Also in this case, the dominant scattering contributions from monopolar and dipolar orders are suppressed, and the residual scattering, much smaller in amplitude, is dominated by higher-order multipoles.

After having shown that an ideal reactive surface may drastically suppress the scattering from a cylinder, we present in the

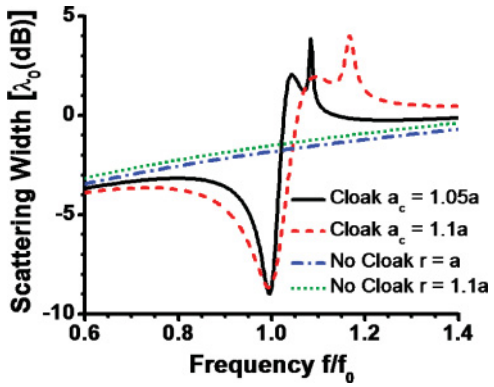

FIG. 7. (Color online) Variation of the total SW of a conducting cylinder, varying the normalized frequency of operation, for mantle cloaks with different ratios a/a_c. The uncloaked conducting cylinders of comparable size are also shown for comparison.

following some realistic designs mantle cloaks based on this concept. We consider first a dielectric cylinder with diameter $2a = \lambda_0/4$ and relative permittivity $\varepsilon = 10$, illuminated by a normally incident TM plane wave. We have used the type-I FSS in Fig. 1(d) to realize the required surface impedance, as from Eq. (4): $a_1 = \lambda_0/5$, $a_c/a = 1.08$, $w_1 = \lambda_0/48$, $\delta_1 = \lambda_0/96$. The metal thickness is $t = \lambda_0/400$, consistent with the 1D geometry (see the inset of Fig. 8 for a sketch of the cloaked geometry).

Figure 8 shows the frequency variation of the total SW for the dielectric cylinder with (solid line) and without (dashed line) the mantle cloak. It is observed that, at the design frequency f_0, the mantle cloak provides drastic scattering reduction, despite its extreme thinness ($\lambda_0/400$). The bandwidth of operation has not been optimized here, and we expect that broader bandwidths may be obtained by using more subwavelength periods and more isotropic patterns, and further reducing the gap between cloak and object, consistent with Fig. 5.

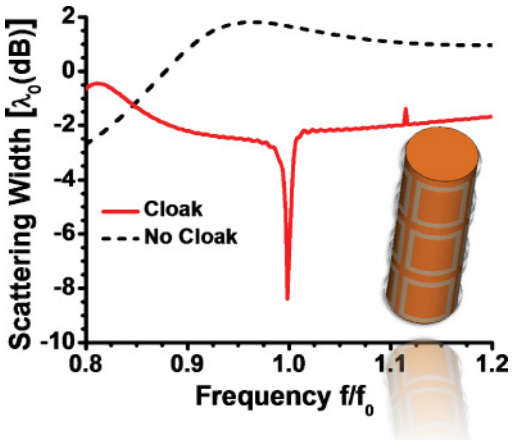

FIG. 8. (Color online) Variation of the total SW of a dielectric infinite cylinder with diameter $2a = \lambda_0/4$ and relative permittivity $\varepsilon = 10$, covered by the metasurface mantle cloak sketched in Fig. 1(b).

Figure 9 shows the corresponding full-wave simulation of the near-field distribution of the electric-field amplitude in the H plane in the case (a) with and (b) without the 2D-cylindrical mantle cloak. It is seen that scattered fields are suppressed in all directions when the mantle cloak is applied. Figure 9(c) shows the power-flow distribution for the cloaked dielectric cylinder, highlighting how most of the plane wave impinging on the cloaked cylinder can tunnel through the mantle cloak without significant perturbation. This is simply obtained by using a properly patterned conducting surface without the need of bulky metamaterial devices. In contrast Fig. 9(d) shows the power-flow distribution without the presence of the mantle cloak, which is highly perturbed by the object showing a significant shadow in the forward direction. A suitable metasurface design, realizing the required uniform surface impedance, allows nearly complete redirection of power flow, making the dielectric cylinder essentially invisible. Unlike transformation-based cloaks, and consistent with the previous analytical results, the full-wave simulations show that a portion of the impinging signal is indeed transmitted inside the mantle cloak, allowing the possibility of extracting part of the signal without necessarily creating a large scattering. This may be beneficial for low-interference communications and cloaked sensing.

Figures 9(e) and 9(f) show the corresponding far-field scattering patterns for the cloaked and uncloaked scenarios, confirming that the designed 2D mantle cloak may suppress the scattering also in the far-field, nearly at all visible angles. A small residual scattering is present in the forward direction, associated with higher-order scattering harmonics. Finally, we point out that our mantle cloak design is not necessarily optimized to minimize the overall scattering: In this work we have limited our design to synthesize the required surface impedance, as from our analytical formulas, focusing on the dominant scattering orders only. More extensive optimization of the metasurface geometry based on global optimization techniques[47,48] may further improve these results, considering the inherent coupling among the object and the surface elements. These concepts go beyond the goal of this paper and will be presented in the near future.

IV. 3D GEOMETRY: SPHERICAL MANTLE CLOAKS

We further extend the previous concepts to a 3D-canonical problem, i.e., plane wave illumination on a spherical object. Figure 1(c) illustrates a dielectric sphere with the diameter $a = \lambda_0/5$ and relative permittivity $\varepsilon = 10$, covered by a concentric mantle cloak with radius $a_c = 1.1a$. Similar to the 2D case, the solution of the boundary-value problem may be approached by expanding the fields in spherical harmonics. The scattering coefficients may be written as[1,45]

$$c_n^{\mathrm{TM}} = -\frac{U_n^{\mathrm{TM}}}{U_n^{\mathrm{TM}} + iV_n^{\mathrm{TM}}},$$
$$c_n^{\mathrm{TE}} = -\frac{U_n^{\mathrm{TE}}}{U_n^{\mathrm{TE}} + iV_n^{\mathrm{TE}}}, \tag{7}$$

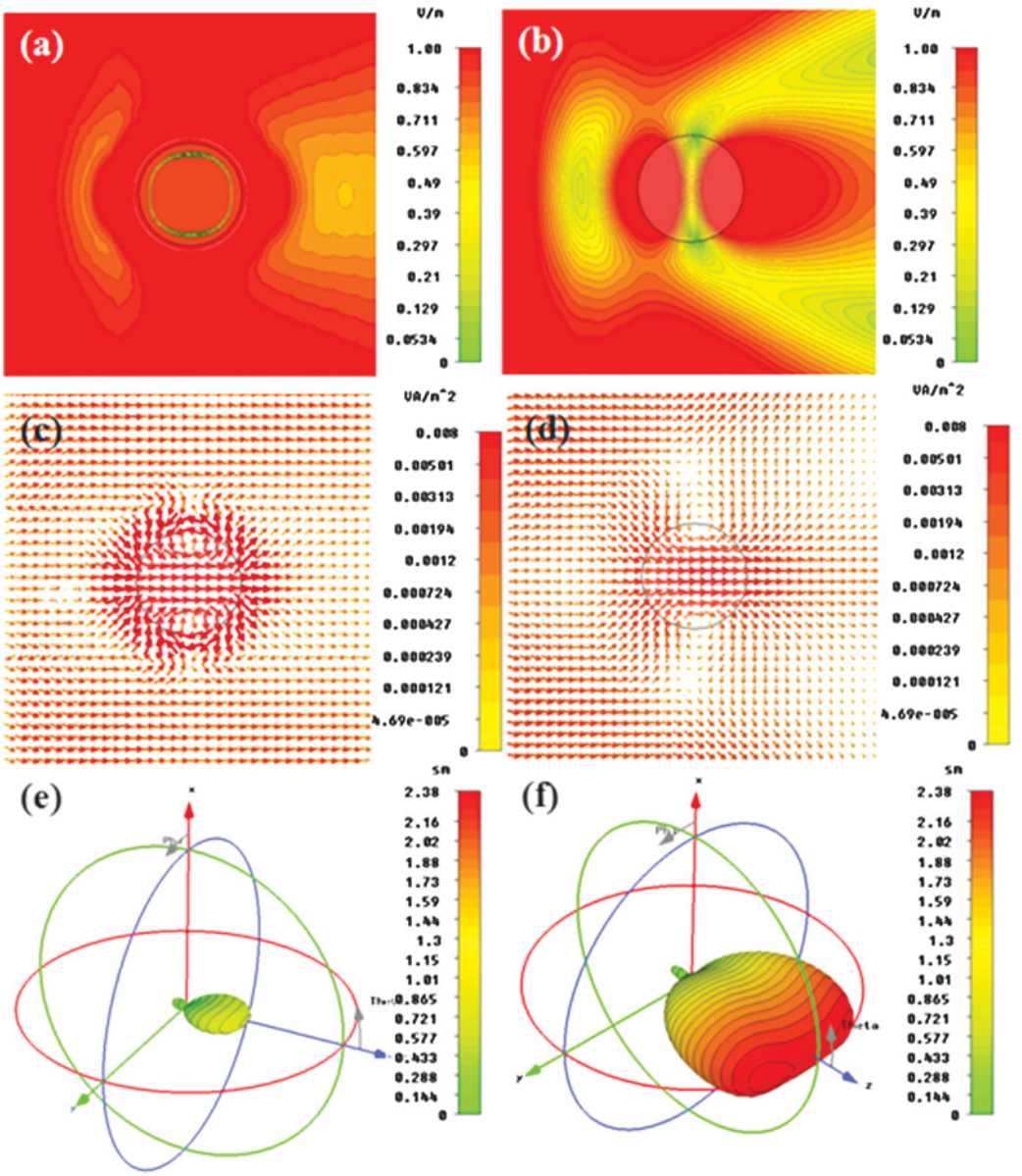

FIG. 9. (Color online) (a) Electric-field amplitude, (c) power-flow distribution, and (e) far-field scattering pattern for a dielectric infinite cylinder with diameter $2a = \lambda_0/4$ covered by a realistic mantle cloak geometry, shown in the inset of Fig. 8. (b), (d), and (f) are similar to (a), (c), and (e), but for the case without cloak.

where U_n^{TM} and V_n^{TM} are given by[23]

$$U_n^{\mathrm{TM}} = \begin{bmatrix} j_n(ka) & j_n(k_0a) & y_n(k_0a) & 0 \\ [ka\, j_n(ka)]'/\varepsilon & [k_0a\, j_n(k_0a)]' & [k_0a\, y_n(k_0a)]' & 0 \\ 0 & \begin{matrix} j_n(k_0a_c)+ \\ +[k_0a_c\, j_n(k_0a_c)]'/(i\omega\varepsilon_0 a_c Z_s) \end{matrix} & \begin{matrix} y_n(k_0a_c)+ \\ +[k_0a_c\, y_n(k_0a_c)]'/(i\omega\varepsilon_0 a_c Z_s) \end{matrix} & j_n(k_0a_c) \\ 0 & [k_0a_c\, j_n(k_0a_c)]' & [k_0a_c\, y_n(k_0a_c)]' & [k_0a_c\, j_n(k_0a_c)]' \end{bmatrix}$$

$$V_n^{\mathrm{TM}} = \begin{bmatrix} j_n(ka) & j_n(k_0a) & y_n(k_0a) & 0 \\ [ka\, j_n(ka)]'/\varepsilon & [k_0a\, j_n(k_0a)]' & [k_0a\, y_n(k_0a)]' & 0 \\ 0 & \begin{matrix} j_n(k_0a_c)+ \\ +[k_0a_c\, j_n(k_0a_c)]'/(i\omega\varepsilon_0 a_c Z_s) \end{matrix} & \begin{matrix} y_n(k_0a_c)+ \\ +[k_0a_c\, y_n(k_0a_c)]'/(i\omega\varepsilon_0 a_c Z_s) \end{matrix} & y_n(k_0a_c) \\ 0 & [k_0a_c\, j_n(k_0a_c)]' & [k_0a_c\, y_n(k_0a_c)]' & [k_0a_c\, y_n(k_0a_c)]' \end{bmatrix}, \quad (8)$$

where $j(\cdot)$ and $y(\cdot)$ are spherical Bessel functions.[42]

For the TE coefficients the dual of Eq. (8) may be easily derived. The total scattering cross section (SCS) in this case is obtained as[43]

$$\sigma_{3D} = \frac{2\pi}{|k_0|^2}\sum_{n=1}^{\infty}\sum_{m=-n}^{n}(2n+1)\left(\left|c_{nm}^{TE}\right|^2+\left|c_{nm}^{TM}\right|^2\right). \quad (9)$$

Similar to the cylindrical case, and consistent with the discussion in Ref. 45, scattering reduction may be obtained by suppressing the U_n coefficients associated with dominant scattering orders, and enhanced resonant scattering may be dually obtained by canceling the V_n coefficients. Both conditions may be achieved with a proper choice of a_c and X_s. In the quasistatic limit, for which $ka, k_0a_c \ll 1$, the dominant contribution to the scattering is usually given by the $n = 1$ harmonics, and approximate conditions for cloaking in the two polarizations are obtained in closed forms as[31]

$$\begin{aligned} \text{TM}: \quad X_s &= \frac{2[2+\varepsilon-\gamma^3(\varepsilon-1)]}{3\gamma^3\omega a\varepsilon_0(\varepsilon-1)} \\ \text{TE}: \quad X_s &= \frac{\omega a\mu_0[2+\mu+2\gamma^3(\mu-1)]}{6\gamma^3(\mu-1)}. \end{aligned} \quad (10)$$

When the size of the object increases, dynamic formulas [Eq. (8)] should be used for the optimal design of the mantle cloak. Figure 10 shows the variation of the total SCS with surface reactance for an ideal mantle cloak surrounding the dielectric sphere. For comparison the case of a bare dielectric sphere (gray-dashed line) is also shown. Similar to the cylindrical geometry for specific surface-reactance values qualitatively consistent with Eq. (10), relevant scattering reduction is obtained for different ratios a_c/a. All mantle cloaks in Fig. 10 display over 95% reduction in the total SCS when the optimal surface reactance values are selected. In addition, for specific surface reactance values, resonant scattering peaks are obtained, corresponding to the dual condition $V_n = 0$ for different values of n and TE or TM scattering coefficients.

Figure 11 shows the frequency response of ideal mantle cloaks considering a dispersionless surface reactance and different radii. In particular, for $a_c = a$ (conformal) the optimal surface reactance, as calculated in Fig. 10, is X_s=70 Ω (black solid line), whereas $X_s = 175\ \Omega$ for

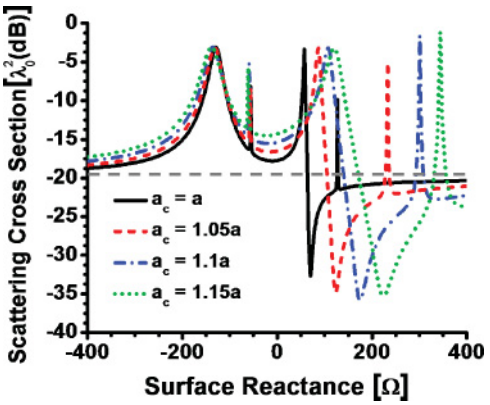

FIG. 10. (Color online) Variation of the total SCS versus surface reactance for a cloaked dielectric sphere with diameter $2a = \lambda_0/5$ and relative permittivity $\varepsilon = 10$; different ratios a_c/a are considered.

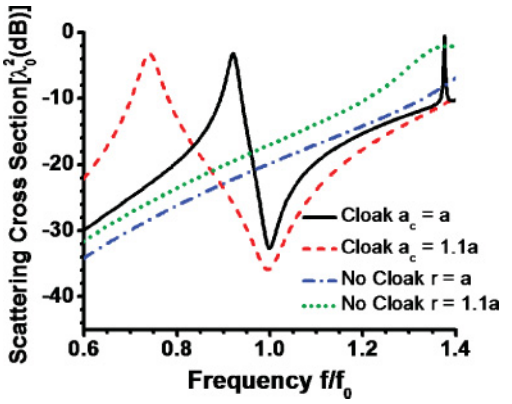

FIG. 11. (Color online) Variation of the total SCS with frequency for a dielectric sphere with diameter $2a = \lambda_0/5$ and relative permittivity $\varepsilon = 10$, covered by a mantle cloak with constant surface reactance, optimized for different ratio a/a_c to suppress the scattering at the design frequency f_0.

$a_c = 1.1a$ (red-dashed line). It is evident that also in this 3D scenario significant scattering reduction may be achieved over a moderately broad range of frequencies, compared with the uncloaked scenarios, without the need of bulk metamaterials.

Figure 12 shows the amplitude of the electric field on the H plane for the dielectric sphere of Figs. 10 and 11, (a) with and (b) without a conformal mantle cloak ($a = a_c$) and optimal surface reactance $X_s = 70\,\Omega$, at frequency f_0 for plane-wave illumination from the left. Figures 11(c) and 11(d) show similar plots for the phase of the magnetic field on the E plane. It is seen that, even for a 3D object, a mantle cloak with suitable surface reactance may drastically suppress the scattering and restore unperturbed planar wavefronts right outside the cloak.

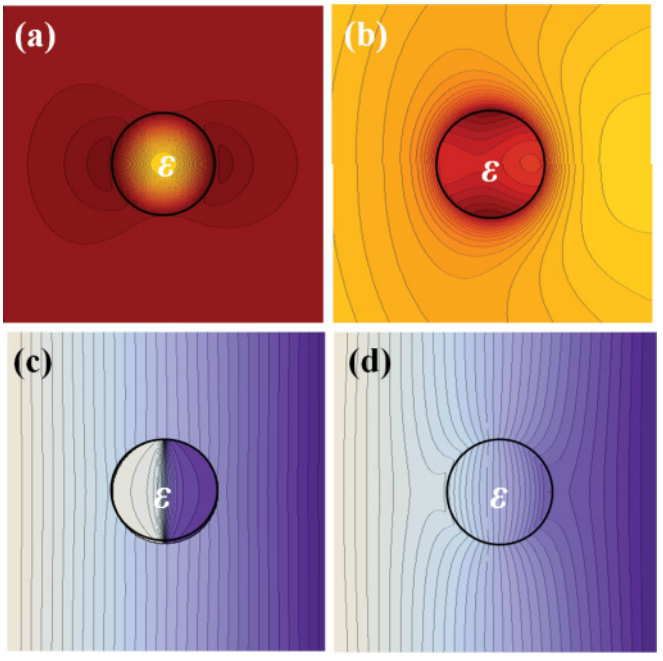

FIG. 12. (Color online) Amplitude of the electric field on the H plane for a dielectric sphere, as in Fig. 11, (a) with and (b) without a conformal mantle cloak. (c) and (d) are similar to (a) and (b), but for the phase of the magnetic field on the E plane.

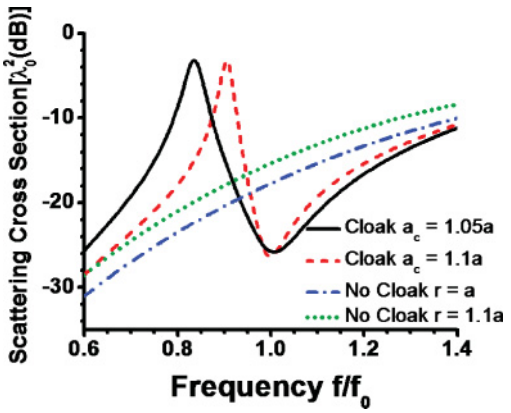

FIG. 13. (Color online) Frequency response of the total SCS for a conducting sphere with diameter $2a = \lambda_0/5$ and relative permittivity $\varepsilon = 10$, covered by the mantle cloaks with different ratio a/a_c.

Also in this case, field penetration inside the sphere may allow cloaked sensing applications.[9]

Consider now the case of a conducting sphere with diameter $2a = \lambda_0/5$ covered by a mantle cloak, analogous to the cylindrical configuration analyzed in Fig. 7. Figure 13 shows analogous results in terms of the total SCS versus frequency. For the case $a_c = 1.1a$ ($a_c = 1.05a$), the overall scattering reduction may reach 86% (87%), with optimal surface reactance $X_s = 92\ \Omega$ ($X_s = 47\ \Omega$). Similar to the cylindrical configuration, the achievable scattering reduction in the conducting scenario is lower than in the dielectric case due to larger contribution from additional multipolar scattering orders and the impenetrability of the object.

Figure 14 shows the amplitude of the electric field on the H plane for a conducting sphere illuminated by a plane wave

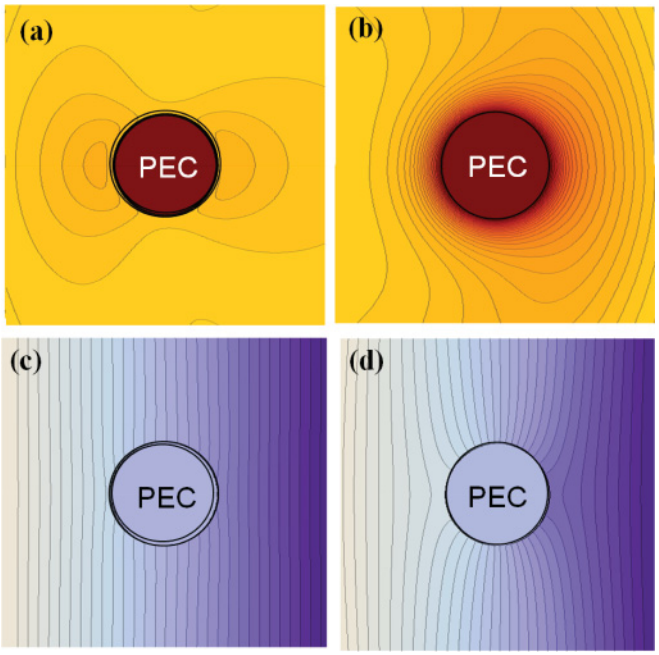

FIG. 14. (Color online) Amplitude of the electric field on the H plane for a conducting sphere (a) with and (b) without the mantle cloak ($a_c = 1.05\,a$) of Fig. 12. (c) and (d) are similar to (a) and (b), but for the phase of the magnetic field on the E plane.

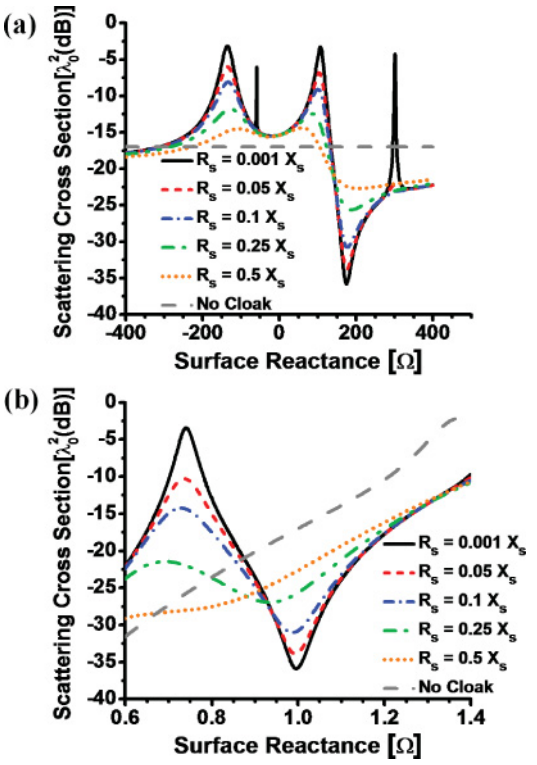

FIG. 15. (Color online) (a) Variation of the total SCS with the surface reactance of a mantle cloak covering the dielectric sphere in Fig. 10, varying the ratio R_s/X_s. (b) Frequency variation of the total SCS for the cloaked dielectric sphere in Fig. 10, but in a lossy scenario for different ratios R_s/X_s.

from the left (a) with and (b) without the mantle cloak of Fig. 13, with radius $a_c = 1.05a$. Figures 14(c) and 14(d) show the phase distribution of the magnetic field on the E plane. Similar features on the restoration of uniform amplitude and planar phase fronts are verified also in this 3D-conducting geometry.

Current cloaks are severely limited by two factors: bandwidth limitations and the impact of losses and imperfections. Although we have shown here that, in principle, the low-profile nature of an ultrathin mantle cloak may moderately improve the bandwidth limitations, its robustness to losses has not yet been discussed.

In Fig. 15 we analyze how the geometry of Fig. 10 is affected by realistic absorption levels by varying the value R_s/X_s, which represents a good figure of merit to assess the relevance of losses in the FSS. Figure 15(a) shows the variation of the total SCS with surface reactance, and Fig. 15(b) shows the variation of SCS versus frequency for a fixed optimal value of X_s, chosen to minimize the scattering at frequency f_0, consistent with the results in Figs. 10 and 11. A moderate increase in surface resistance R_s deteriorates the cloaking effect just weakly, and the optimal value of surface reactance is almost unaffected by moderate losses. This is also seen in the frequency response of Fig. 15(b).

For comparison Figs. 16(a) and 16(b) show the amplitude of the electric field on the H plane for spherical mantle cloaks with surface resistance $R_s = 0.1X_s$ and $R_s = 0.25X_s$, respectively, where the value of X_s is the same as the one

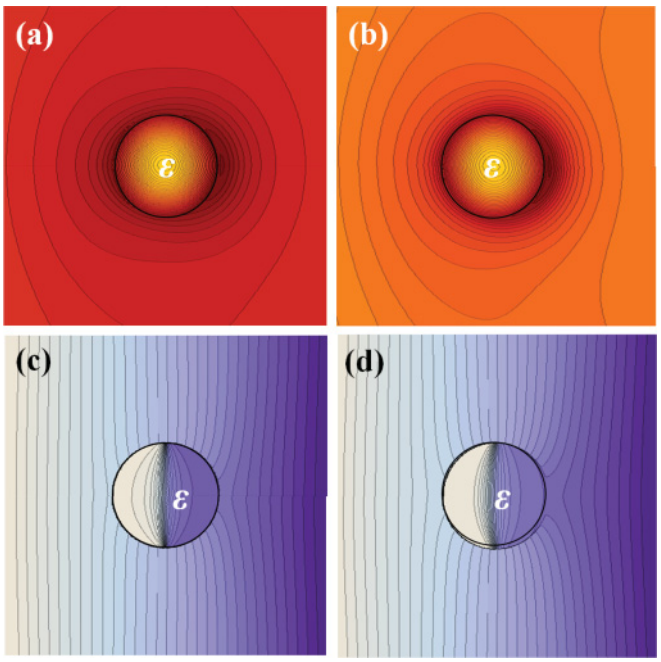

FIG. 16. (Color online) Amplitude of the electric field on the H plane for the cloaked dielectric sphere in Fig. 11, with normalized surface resistance (a) $R_s = 0.1X_s$ and (b) $R_s = 0.25X_s$. (c) and (d) are similar to (a) and (b), but for the phase of the magnetic field on the E plane.

used in Fig. 15(b), optimized to suppress the scattering at the design frequency. The effect of losses is somewhat visible in the near-field distributions, but the cloaking phenomenon is still evident. The inherent robustness of mantle cloaks to losses is consistent with the robust performance highlighted for the plasmonic cloaking technique, which is based on similar scattering cancelation effects.[29] Figures 16(c) and 16(d) show the phase of the magnetic field on the E plane with similar results. Different from the cloaking scenario, the resonant-scattering peaks associated with the cancelation of V_n for specific reactance values are largely affected by losses (Fig. 15), as expected due to the resonant nature of this dual phenomenon.

We consider now realistic mantle cloak designs to suppress the scattering from a 3D-dielectric sphere with diameter $2a = \lambda_0/3$ at frequency f_0 and relative permittivity $\varepsilon = 10$,

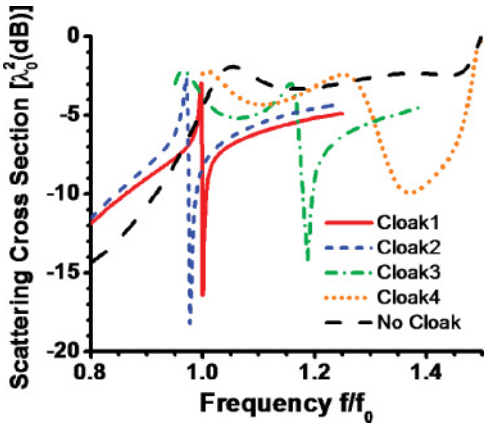

FIG. 18. (Color online) Frequency response of the total SCS for a dielectric sphere covered by different realistic mantle cloaks, with geometries shown in Fig. 17.

as sketched in Fig. 1(c). Figure 17 shows various mantle cloak geometries that we have considered in our design, providing different surface reactances suitable to suppress the scattering at different frequencies; the scale bar in the figure represents a length of $\lambda_0/10$ at frequency f_0. Figure 18 shows the corresponding total SCS calculated for these geometries, varying the frequency of operation. It is evident how, by modifying the metasurface geometry and its periodicity, it is possible to tune the cloaking frequency up to wavelengths comparable and smaller than the size of the object of interest (cloak 4 in Fig. 17). Many of these designs have been in purpose tailored to be quasi-isotropic, ensuring independent response for all incidence angles and polarizations.

Figures 19(a) and 19(b) show the amplitude of the total electric field for a dielectric sphere with diameter $2a = 2\lambda/5$ (here $\lambda = \lambda_0/1.2$ is the cloaking wavelength for this design) with and without the presence of a type-3 cloak in Fig. 17, which is composed of type-II FSS as in Fig. 1(d) with design parameters $a_2 = \lambda_0/3.2$, $a/a_c = 1.08$, $w_2 = \lambda_0/37.5$, $\delta_2 = \lambda_0/30$, and cloak thickness $t = \lambda_0/400$. Also in this 3D geometry, it is verified that a properly designed mantle cloak may considerably suppress the scattered fields in all directions in the near- and far-field. Figures 19(c) and 19(d) show the power-flow distribution for the dielectric sphere with and without mantle cloak, respectively, confirming how most of the energy impinging on the cloaked sphere can

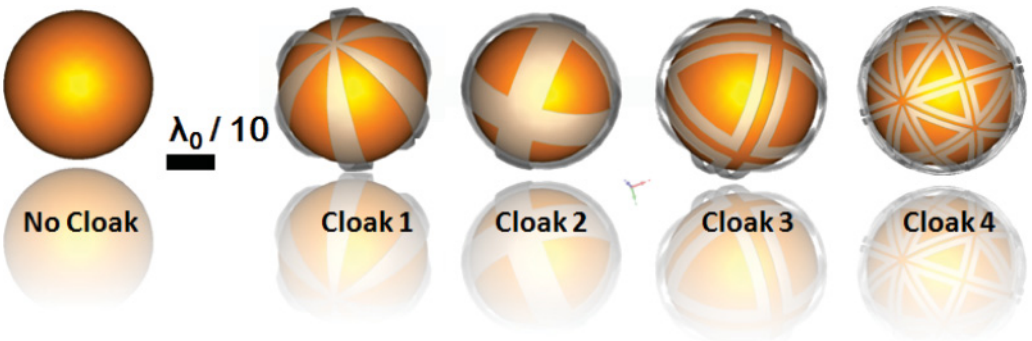

FIG. 17. (Color online) Practical mantle cloak designs for a dielectric sphere with diameter $2a = \lambda_0/3$, at frequency f_0, as considered in the examples of Sec. IV

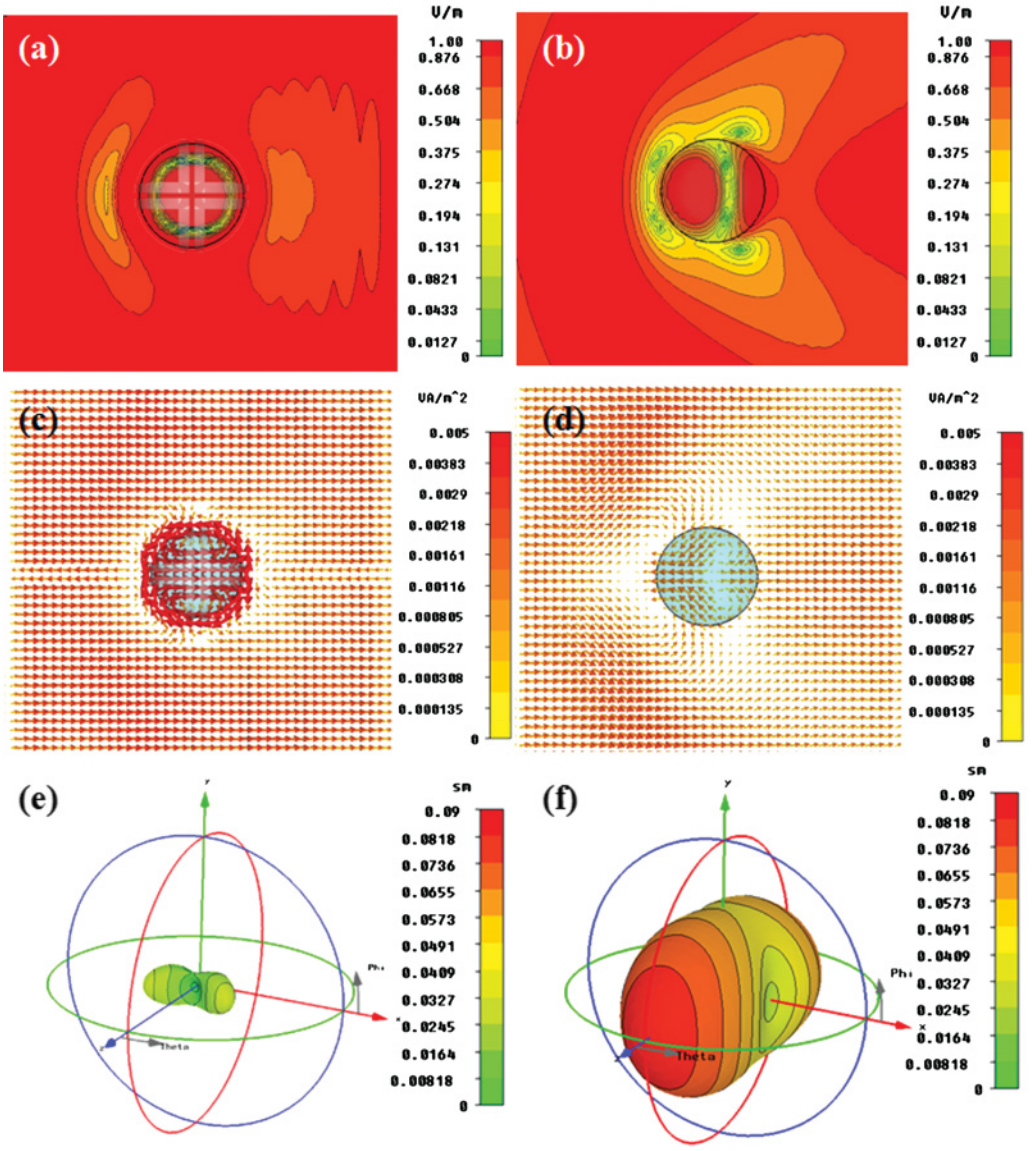

FIG. 19. (Color online) (a) Electric-field amplitude, (c) power-flow distribution, and (e) far-field radiation pattern for a dielectric sphere covered by cloak type-3 in Fig. 17. (b), (d), and (f) are similar to (a), (c), and (e), but for a dielectric sphere of same size $2a = 2\lambda/5$. without cloaking.

tunnel through the mantle cloak without causing perturbations. Finally, Figs. 18(e) and 18(f) show the far-field scattering pattern for the dielectric sphere with and without mantle cloak, respectively, confirming that the scattering is largely suppressed also in the far-field of the object and at all angles.

We further consider the design of mantle cloaks operating at larger frequencies, for which the considered dielectric sphere has a diameter $2a \sim \lambda/2$ (i.e., $\lambda = \lambda_0/1.5$), by adapting the density and periodicity of metallic patterns producing type-4 cloak in Fig. 17. This cloak is composed of type-II FSS, similar to the previous design, but with different design parameters: $a_2 = \lambda_0/5$, $a/a_c = 1.08$, $w_2 = \lambda_0/60$, $\delta_2 = \lambda_0/150$. Figures 20(a), 20(c), and 20(e), respectively, show the amplitude of the electric field, power-flow distribution, and far-field radiation pattern for a dielectric sphere covered by the designed cloak. Similar results for the bare dielectric sphere are shown in Figs. 20(b), 20(d), and 20(f) for comparison. Despite the larger electrical size, the cloaking effect is still excellent. Comparing the power-flow distribution in the cloaked and uncloaked scenarios, it is found that the backward scattering and shadow regions are dramatically suppressed by this realistic 3D mantle cloak geometry.

The far-field scattering patterns for the cloaked [Fig. 20(e)] and uncloaked [Fig. 20(f)] spheres confirm the drastic scattering suppression in this scenario, which amounts to an overall SCS reduction of over 90%. These results show that it is indeed possible to employ simple FSS designs to realize mantle cloaks tunable over a wide range of frequencies and easily tailored for various metasurface geometries and designs. Similar concepts may be employed to realize the dual of this phenomenon, i.e., resonant-scattering enhancement in specific frequency ranges, in particular for smaller objects, for which the scattering enhancement may be more dramatic, which is consistent with Ref. 44. Physical insights and potential applications of

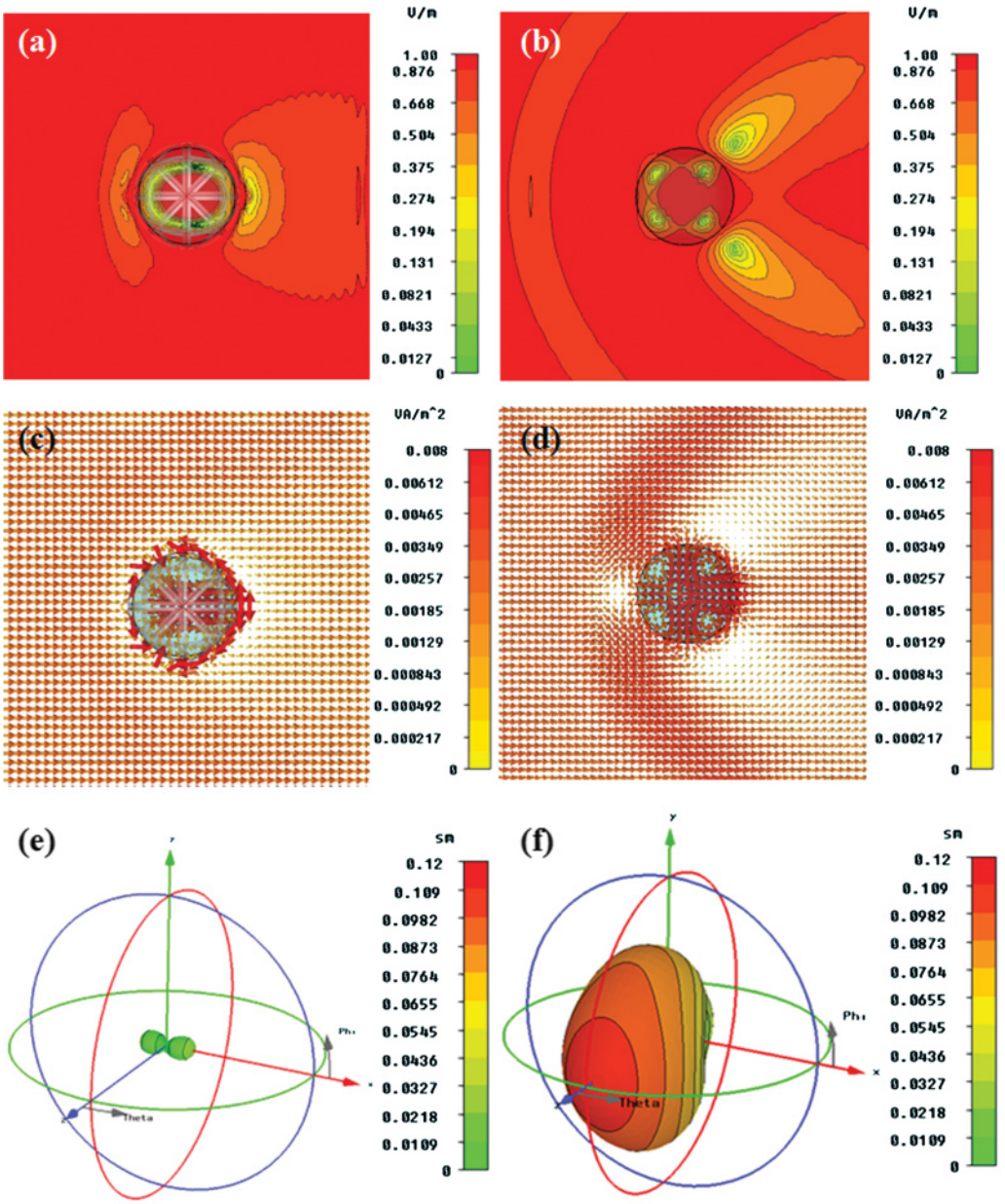

FIG. 20. (Color online) (a) Electric-field amplitude, (c) power-flow distribution, and (e) far-field radiation pattern for a dielectric sphere with mantle cloak type-4 (see Fig. 17). (b), (d), and (f) are similar to (a), (c), and (e), but for a dielectric sphere without cloaking. The sphere has normalized diameter $2a = \lambda/2.15$.

this dual phenomenon, including the enhancement of antenna gain and the realization of subwavelength resonant inclusions for metamaterials using ultralow-profile metasurfaces, will be addressed in future work.

V. CONCLUSIONS

We have analyzed here the theoretical possibility and practical implementation of mantle cloaks for 1D, 2D, and 3D objects. We have discussed analytical and full-wave simulations, physical insights, and potential applications of the mantle cloaking technique in realistic configurations. The presented results may be beneficial not only for invisibility and camouflaging applications, but also for noninvasive probing, sensing, imaging, and low-interference communications. We envision that established FSS technology may be applied to readily realize ultrathin, low-profile, inexpensive, and moderately broadband cloaks, thus largely accelerating the possibility of realizing efficient cloaking devices. These same concepts may be extended to THz frequencies and to multilayered configurations for enhanced bandwidth, multifrequency operation, and to cloak larger objects. In this context a THz mantle cloak formed by a graphene monolayer has been proposed in Ref. 49.

ACKNOWLEDGMENT

This work has been supported by NSF with a CAREER Grant No. ECCS-0953311.

*alu@mail.utexas.edu

[1] A. Alù and N. Engheta, Phys. Rev. E **72**, 016623 (2005).
[2] J. B. Pendry, D. Schurig, and D. R. Smith, Science **312**, 1780 (2006).
[3] D. Schurig, J. J. Mock, B. J. Justice, S. A. Cummer, J. B. Pendry, A. F. Starr, and D. R. Smith, Science **314**, 977 (2006).
[4] U. Leonhardt, Science **312**, 1777 (2006).
[5] G. W. Milton and N. A. Nicorovici, Proc. R. Soc. A **462**, 3027 (2006).
[6] W. Cai, U. K. Chettiar, A. V. Kildishev, and V. M. Shalaev, Nat. Photonics **1**, 224 (2007).
[7] A. Alù and N. Engheta, J. Opt. A **10**, 093002 (2008).
[8] A. Alù and N. Engheta, Phys. Rev. Lett. **100**, 113901 (2008).
[9] A. Alù and N. Engheta, Phys. Rev. Lett. **102**, 233901 (2009).
[10] M. G. Silveirinha, A. Alù, and N. Engheta, Phys. Rev. E **75**, 036603 (2007).
[11] B. Edwards, A. Alù, M. G. Silveirinha, and N. Engheta, Phys. Rev. Lett. **103**, 153901 (2009).
[12] S. Tretyakov, P. Alitalo, O. Luukkonen, and C. Simovski, Phys. Rev. Lett. **103**, 103905 (2009).
[13] G. Castaldi, I. Gallina, V. Galdi, A. Alù, and N. Engheta, Opt. Express **17**, 3101 (2009).
[14] Y. Luo, J. Zhang, H. Chen, L. Ran, B. Wu, and J. A. Long, IEEE Trans. Antenna Propagat. **57**, 3926 (2009).
[15] J. Valentine, J. Li, T. Zentgraf, G. Bartal, and X. Zhang, Nat. Mater. **8**, 568 (2009).
[16] T. Ergin, N. Stenger, P. Brenner, J. B. Pendry, and M. Wegener, Science **328**, 337 (2010).
[17] J. Valentine, S. Zhang, T. Zentgraf, E. Ulin-Avila, D. A. Genov, G. Bartal, and X. Zhang, Nature **455**, 376 (2008).
[18] Y. Liu, T. Zentgraf, G. Bartal, and X. Zhang, Nano Lett. **19**, 1991 (2010).
[19] X. Chen, Y. Luo, J. Zhang, K. Jiang, J. B. Pendry, and S. Zhang, Nature Commun. **2**, 176 (2011).
[20] B. Zhang, Y. Luo, X. Liu, and G. Barbastathis, Phys. Rev. Lett. **106**, 033901 (2011).
[21] A. Greenleaf, Y. Kurylev, M. Lassas, and G. Uhlmann, Comm. Math. Phys. **275**, 749 (2007).
[22] A. Greenleaf, Y. Kurylev, M. Lassas, and G. Uhlmann, Phys. Rev. E **83**, 016603 (2011).
[23] A. Alù, Phys. Rev. B **80**, 245115 (2009).
[24] P. Y. Chen and A. Alù, *IEEE Int. Sym. Antennas and Propagat.*, Toronto, Canada, July 11–17 (2010).
[25] F. Zambonelli and M. Mamei, IEEE Pervasive Comput. **1**, 62 (2002).
[26] D. A. B. Miller, Opt. Express **14**, 12457 (2006).
[27] D. H. Kwon and D. H. Werner, *IEEE Antenna Propagat. Soc. Int. Sym.*, San Diego, July (2008).
[28] D. H. Kwon and D. H. Werner, Appl. Phys. Lett. **92**, 113507 (2008).
[29] A. Alù and N. Engheta, Opt. Express **15**, 7578 (2007).
[30] A. Alù and N. Engheta, Opt. Express **15**, 3318 (2007).
[31] A. Alù, Phys. Rev. B **83**, 081102(R) (2011).
[32] A. Alù, Phys. Rev. B **84**, 075153 (2011).
[33] A. Alù and N. Engheta, Phys. Rev. E **78**, 045602(R) (2008).
[34] E. Kallos, C. Argyropoulos, Y. Hao, and A. Alù, Phys. Rev. B **84**, 045102 (2011).
[35] B. A. Munk, *Frequency Selective Surface: Theory and Design* (John Wiley and Sons, New York, 2000).
[36] L. B. Whitbourn and R. C. Compton, Appl. Opt. **24**, 217 (1985).
[37] J. McVay and N. Engteta, IEEE Microwave Wireless Comp. Lett. **14**, 130 (2004).
[38] CST Microwave Studio [http://www.cst.com].
[39] J. A. Gordon, C. L. Holloway, and A. Deinstfrey, IEEE Antennas Wireless Propag. Lett. **8**, 1127 (2009).
[40] Y. Zhao, N. Engheta, and A. Alù, Metamaterials **5**, 90 (2011).
[41] A. Alù, D. Rainwater, and A. Kerkhoff, New J. Phys. **12**, 103028 (2010).
[42] M. Abramowitz and I. A. Stegun (eds.), *Handbook of Mathematical Functions with Formulas, Graphs, and Mathematical Tables*, 9th printing (Dover, New York, 1972), pp. 355–435.
[43] C. F. Bohren and D. R. Huffman, *Absorption and Scattering of Light by Small Particles* (Wiley, New York, 1998), pp. 287–289.
[44] It may also be possible to realize the dual of this effect, consistent with the concepts introduced in Ref. 45: we may envision zeroing the determinant Q_l^{TM}, obtaining resonant response for the lth TM cylindrical scattering harmonic ($c_l^{TM} = -1$ in the lossless scenario), which corresponds to resonant scattering. This would be similar to the resonant properties of a subwavelength nanoparticle suitably coated by a plasmonic material.[46] Also in this case, the anomalous scattering may be conveniently supported by an ultrathin surface.
[45] A. Alù and N. Engheta, J. Appl. Phys. **97**, 094310 (2005).
[46] A. Alù and N. Engheta, IEEE Trans. Antenna Propagat. **55**, 3027 (2007).
[47] P. Y. Chen, C. H. Chen, and H. Wang, Appl. Comput. Intell. Soft Comput. **1**, 474125 (2009).
[48] P. Y. Chen, C. H. Chen, H. Wang, J. H. Tsai, and W. X. Ni, Opt. Exp. **16**, 12806 (2008).
[49] P. Y. Chen and A. Alù, ACS Nano **5**, 5855 (2011).